Infrared Spectroscopy of Human Cells and Tissue. VIII. Strategies for Analysis of Infrared Tissue Mapping Data and Applications to Liver Tissue

MAX DIEM,[1] LUIS CHIRIBOGA,[1] [2] HERMAN YEE[2]

[1] Department of Chemistry and Biochemistry, City University of New York, Hunter College, 695 Park Avenue, New York, New York 10021

[2] Department of Pathology, Bellevue Hospital and New York University Medical Center, 27th Street and First Avenue, New York, New York 10016

ABSTRACT: Experimental and computational methods of infrared microspectroscopy (IRI-MSP) and infrared spectral mapping (ISM) are presented. These methods are subsequently applied to the analysis of cirrhotic liver tissue. The sensitivity of infrared spectral mapping toward spectral changes caused by disease will be demonstrated. In addition, the excellent agreement between ISM data and histopathological information will be discussed. © 2000 John Wiley & Sons, Inc. Biopolymers (Biospectroscopy) 57: 282–290, 2000

Keywords: IR microspectroscopy; human cells and tissue; tissue mapping

INTRODUCTION

IR microspectroscopy (IR-MSP), also referred to as IR microscopy, offers the opportunity to collect spectral data from entities the size of single cells or from pixels of tissue of similar size. This capability, coupled with the ability of IR spectroscopy to distinguish between different tissue types and between the states of health, maturation, and differentiation of cells, has opened the doors for applications of IR spectroscopy in pathology and cytology.[1,2] For example, we demonstrated in two recent articles that IR-MSP distinguishes between normal, cirrhotic, and cancerous liver tissue specimens. A detailed correlation between histopathological, immunohistochemical, and spectral analyses of these samples provided insight into the changes in chemical and biological compositions that occur when normal tissue transforms into diseased tissue.[3,4] In those two articles we dealt with spectral information collected from individual spots with distinct pathological information, but here we present data collected as *IR spectral maps* from large sections (ca. $7 \times 2 \text{ mm}^2$) of tissue and discuss the pathological information that is contained in such maps.

IR spectral maps can be collected using an IR microspectrometer with a single detector element and an adjustable microscope aperture to select an area from which spectral data are to be obtained. Subsequently, the sample is moved in a raster pattern in increments of about the same size as the optical aperture.[5,6] In this way a map of IR spectral data may be acquired. This method

is commonly referred to as *IR spectral mapping*. Alternatively, the optical aperture may be omitted, and the single detector element can be replaced by an array detector. In this case, the spatial resolution is determined by the size of each individual detector element; spatial resolutions of about 4–10 μm have been achieved.[7,8] Following previous literature, we refer to this methodology as *IR spectral imaging*. We contrast, in this context, the terminology IR spectral imaging against IR imaging as described by Freeman.[9] "Thermal" pictures of tissue or organs were reported in the IR images without the use of a spectrometer or any other wavelength discriminating element.

In this article we concentrate on three distinct areas. The first is a summary of our data acquisition strategy, and the second is a discussion of the data analysis method to create the IR spectral maps. This method differs significantly from the mathematical approaches used by others[5,6] to obtain spectral maps in that our approach emphasizes compositional (chemical) changes that occur between microscopic areas of tissue. Therefore, our approach is ideally suited for correlation with histochemical data. In the third area we demonstrate the power of this approach by analyzing sections of cirrhotic liver tissue in which spectral changes on the microscopic level agree extremely well with known histopathology.

MATERIALS AND METHODS

Sample Preparation

Samples are prepared as follows for spectral tissue mapping. A 4-μm tissue section was cut from paraffin-embedded tissue blocks, mounted on a glass slide, and stained with hematoxylin and eosin (H&E). Next a 6-μm tissue section was cut and mounted onto a barium fluoride disk (19-mm diameter) or a rectangular (19 $\times$ 38 mm^2) barium fluoride window. Sections were subsequently deparaffinized, rehydrated, and allowed to air dry. Other groups used tissue sections produced from frozen blocks, and they obtained spectra that are essentially identical to the spectra reported here.[6]

Regions of interest were identified using the H&E stained section and a high quality (visible range) microscope. Corresponding features were identified by anatomical landmarks on the unstained tissue sections; subsequently, the tissue section was transferred to the IR microscope and aligned using the anatomical landmarks.

Data Acquisition

Data presented here were collected via a Bruker IRScope II IR microscope (Bruker Optics, Inc., Billerica, MA) equipped with a liquid nitrogen cooled HgCdTe detector, 15$\times$ and 36$\times$ IR objectives, and a CCD camera for capture of visual images. The IRScope II was coupled to a Bruker Vector 22 Fourier transform IR (FTIR) spectrometer. The combination of these instruments, henceforth referred to as the IR microspectrometer, was controlled by a personal computer (Gateway 2000) incorporating a 200-MHz Pentium processor running under OS/2 Warp. Data collection was carried out using Bruker's proprietary OPUS (version 3.0) software.[10]

The IRScope II and the FTIR spectrometer were continually purged with dry air from self-contained air purifiers (Whatman, Inc.) The working area of the IRScope II, including the focal plane, was enclosed in a plastic skirt to provide easy access and the possibility of good purging.

The IR microscope permitted the selection of rectangular apertures of between 5 and about 200 μm on edge. However, because of light throughput limitations, apertures smaller than 20 $\times$ 20 μm^2 were found to be impractical. The data reported here were collected for a square aperture that was 75, 50, or 33 μm on edge. The selected aperture was calibrated against a standard, rectangular aperture image calibrated in 10-μm increments. The aperture sizes reported are thought to be accurate to about ± 3 μm.

The IR mapping data were collected by scanning the computer controlled microscope stage in a raster pattern in increments corresponding to the aperture size. At each data point a preset number of interferograms was coadded, depending on the aperture selected: $\sim$100 interferograms for 33 $\times$ 33 μm^2, 32 interferograms for 50 $\times$ 50 μm^2, and 6 interferograms for 75 $\times$ 75 μm^2 were found to produce the signal-to-noise (S/N) ratio required for subsequent analysis. Interferograms were collected double sided at a resolution of 4 cm^{-1} with a zero-filling factor of 4, which are spectral data points spaced at about 0.9645 cm^{-1}. The quality of data is of the utmost important for the subsequent analysis. The spectrum shown in Figure 1 is typical of the quality of data required for subsequent analyses; furthermore, it exhibits

the typical shape of tissue spectra of between about 700 and 4000 cm^{-1}.

Spectral Data Manipulation: Preprocessing

For mapping experiments, the Bruker OPUS software[10] creates and stores one large file that contains all spectra for a given mapping area. Individual spectra for each pixel point are extracted from this map by a procedure called "postrun extraction". The extracted spectra were converted to a more compact data format developed in our laboratory and stored for further processing that is referred to as "data preprocessing". This preprocessing includes expansion, water vapor subtraction, background correction, smoothing, straight-line generation, and storage in a compact format suitable for subsequent calculations. These operations are now discussed in more detail.

Figure 1 shows a typical raw spectrum for a 50 $\times$ 50 μm^2 section of 6 μm thick liver tissue. The overall spectral shapes (i.e., the strong scattering background above 2000 cm^{-1}, the broad NH and OH stretching vibrations, and the strong amide I and II peaks at 1550 and 1650 cm^{-1}, respectively) are typical of spectra of most cells and tissues.

Although the microspectrometer is enclosed and purged continuously, the water vapor vibrotational spectrum may interfere with the amide I band of the cells and tissues. Because the sample spectrum is ratioed against a water vapor background spectrum stored as the I_0 trace for the
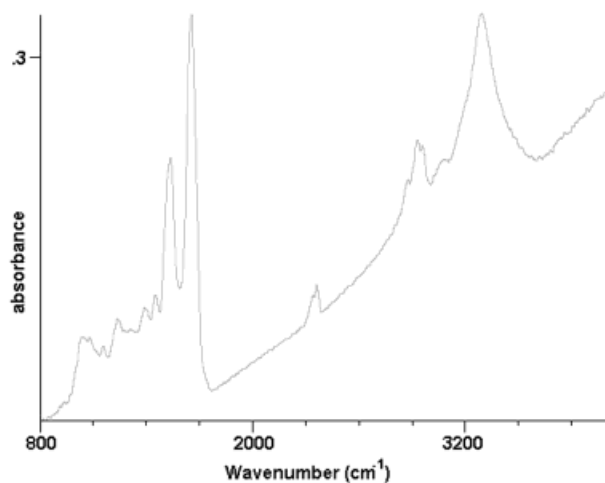

Figure 1. A raw IR-MSP spectrum of a 50 $\times$ 50 μm^2 section of 6 μm thick liver tissue at 4 cm^{-1} spectral resolution for six coadded interferograms.

computation of transmission or absorption spectra, the resulting water vapor interference is generally smaller than the amide I peak. However, mapping experiments that take more than 10 h often exhibit positive or negative water vapor spectral features because it is virtually impossible to maintain a constant humidity level in the sample area of the microspectrometer over that length of time. This problem is particularly significant if data are collected at a resolution equal to or better than 2 cm^{-1}.

Therefore, we developed an algorithm to automatically correct the water vapor background. The discussion of this part of this program is outside the intended scope of this article and will be reported in the future.[11]

After water vapor subtraction, data are background corrected by an algorithm modeled after the "rubber band" method contained in the Bruker OPUS package.[10] Conceptually, this algorithm can be described as stretching a rubber band from below a spectrum and drawing a baseline between all points where the rubber band touches the spectrum. For the spectral region between 800 and 1800 cm^{-1}, the background changes uniformly as shown in Figure 1; therefore, the rubber band algorithm fits a straight line between the two lowest points of the spectrum at 800 and 1800 cm^{-1}. It is clear that any background correction may introduce errors in band shapes and intensities; however, we found that the straight-line background correction does not introduce sigificant artifacts, particularly because most of the subsequent data analysis is performed in second derivative space, in which broad background features are eliminated.

The spectral data may be smoothed by a 5-, 9-, 15-, or 25-point Savitzky–Golay smoothing function.[12] Given the width of the peaks in typical tissue data, the loss of resolution is negligible. Finally, a straight-line generator is available to remove any remaining substrate peaks, for example, if polyethylene is used as a sample substrate. For barium fluoride or zinc selenide windows, the straight-line generator is not utilized.

The preprocessing program requires about 0.2 s of data processing time for each spectrum on a 450-MHz Pentium II processor. The iterative water vapor subtraction, which may require 100 or more fitting cycles, increases this processing time to about 1 s/spectrum. The program operates completely unsupervised and has been used to process well over 250,000 individual spectra.
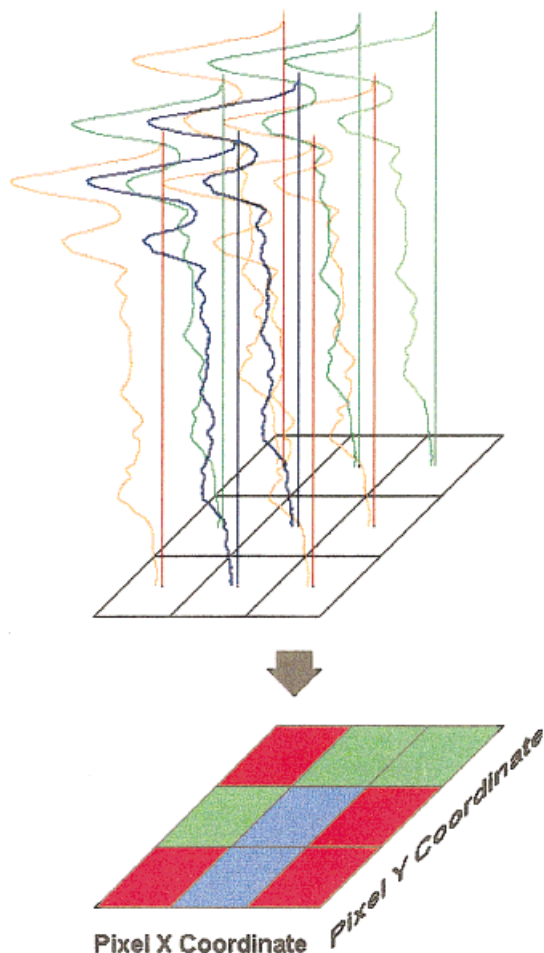
Figure 2. A schematic representation of the data reduction algorithm. Top: A 4-dimensional representation of raw data in which the dimensions for each pixel point are pixel coordinates X and Y, the wavenumber axis, and the intensity axis. Bottom: A false color representation of the same spectral data.

Spectral Data Manipulation: Spectral Correlation and Clustering

Spectral mapping or spectral imaging data are obtained in the format of a "spectral hypercube" of N spectral vectors, each consisting of M wavenumbers versus the intensity values. Here N is the product of N_x columns and N_y rows of pixels. This is shown schematically in Figure 2.

Several methods exist to convert this hypercube into a 2-dimensional visualization. The easiest way to visualize the spectral data from the hypercube is to present "horizontal" slices through the hypercube, which displays intensity values at a given wavenumber for all spectral vectors as a false color representation. The intensity value of each spectrum is assigned a color code and displayed against the X and Y coordinates of the spectral element. By examining different "color slices" (i.e., the intensities at different spectral elements), variations in the chemical composition can be detected for various pixels in the hypercube.

Such color slice displays can be coupled to software that permits comparison of intensity ratios or ratios of integrated band intensities. In this manner, confounding factors such as variations in thickness of the sample can be accounted for, because data can be normalized to a given spectral region. In tissue spectroscopy the integrated amide I intensity may be used advantageously as an internal standard of intensities.

More sophisticated ways to analyze spectral hypercube data have been reported as well.[5,6,13] Among them are principle component (PC) analysis based methods utilized by Lewis[13] and Lasch and Naumann.[5] In this approach the magnitude of scores corresponding to the different loading vectors are color coded and plotted against the X and Y pixel coordinates. This method has the advantage of emphasizing the change in spectra, because PC analysis is designed to emphasize spectral variations; however, the resulting loading vectors are physically meaningless. This may be alleviated by a computational method of "successive transformation factor analysis" that transforms the spectral vectors of maximal change to physically significant basis vectors of chemical components by relaxing the constraints of orthogonality on the loading vectors.[14]

We present a data analysis method that consists of establishing the similarity, or relatedness, of spectra and establish for each class of related spectra the "most characteristic" spectrum. The goal of the data processing effort is to produce an easily interpretable, false color map from the spectral data that may be correlated to the results obtained from standard pathology and histopathology. As such, the data manipulation program reduces the data from a 4-dimensional spectral display into a more manageable, 2-dimensional map. This process is shown schematically in Figure 2.

The spectral data set is analyzed for the similarity between all spectra. This similarity is expressed by a similarity index via one of two methods: one of them is simply the Euclidean[15] distance between spectra, defined as [eqs. (1) and (3) are given in Ref. 15 with several square and square root symbols misplaced]

$$C_{SR} = \frac{\Sigma_i S_i R_i}{\sqrt{\Sigma_i (S_i)^2} \sqrt{\Sigma_i (R_i)^2}} \quad [i = 1\cdots M] \quad (1)$$

where S_i is a 1-dimensional vector of spectral intensities of the sample spectrum for M equidistant data points and R_i is a corresponding "reference" spectral vector. In this approach every spectral vector serves as a reference to all other spectra (i.e., the matrix C_{SR} contains N^2 entries, where N is the total number of spectra in a data set) with

$$N = N_x \cdot N_y \quad (2)$$

The S_i and R_i need to be normalized; therefore, the "overlap" C_{SR} between a spectrum and a reference ranges from 1.0 for a perfect fit to 0.0 for no fit.

Alternatively, unnormalized but mean-centered vectors S_i and R_i may be used. The resulting overlap in this case is referred to as the "vector correlation" and is given by[15]

$$C_{SR} = \frac{\Sigma_i (S_i - \bar{S})(R_i - \bar{R})}{\sqrt{\Sigma_i (S_i - \bar{S})^2} \sqrt{\Sigma_i (R_i - \bar{R})^2}} \quad (3)$$

Here $\bar{S}$ and $\bar{R}$ are the average values of each vector. We use the vector correlation algorithm mostly with second derivative data, which are approximately zero centered. The second derivatives were used by many research groups (e.g., Helm et al.)[16] to correlate spectra, because second derivatives are very sensitive to the number and positions of component bands in broad spectral envelopes.

Because the matrix element C_{SR} is calculated for all pairs of spectra, the computations involved are quite time consuming. To speed up the computations, all sums in the denominator of eqs. (1) or (3) are calculated once for each spectrum and stored with each spectral vector. Consequently, only the inner product [the numerators of eq. (1) or (3)] of the vectors needs to be recomputed for each element. Furthermore, because C_{SR} is symmetric, only the upper half of it needs to be computed. On a moderately fast personal computer, the inner product calculation can be accomplished in about 0.5 ms for two 1000-point vectors; thus, computation of the C_{SR} matrix for a 2000 spectra data set may take about 20 min.

Subsequently, the C_{SR} matrix is analyzed as follows to identify related spectra and to deter-mine the "characteristic spectra." The C_{SR} matrix is scanned for the one column with the highest average value of C. The spectrum A corresponding to this column is referred to as the first characteristic spectrum. The elements (scores) in column A of the C_{SR} matrix [i.e., the elements C_{SA} ($S = 1\cdots N$)] are sorted by decreasing magnitudes. These scores exhibit distinct "steps" when a spectrum S correlates less well with spectrum R than previous spectra. The position of the first step, determined computationally via differentiation of the score versus the spectral number, is used as a cutoff point to select spectra that fall into the family of spectra related to the characteristic spectrum A. Subsequently, all rows and columns of spectra related to spectrum A are zeroed in the C_{SR} matrix. This process is repeated until the entire C_{SR} matrix is zero.

The advantage of this computational approach is that it operates unsupervised: no prior knowledge of reference spectra of any tissue type is required, and characteristic spectra and membership of the families of spectra identified by the characteristic spectra are established, regardless of the number of different spectral families and the differences between spectral families. The method described here uses a large portion of the spectrum, rather than a few selected points, regions, or integrated regions, to determine whether spectra are related or not. Because the differences between spectra of normal and diseased tissue are generally small, this method offers the advantage of emphasizing differences in the overall shape, rather than selected intensities, for the discrimination of spectra.

In the final step all spectra in the same family are assigned a color code, and small, colored squares are drawn at the pixel coordinates of all spectra belonging to the same family to produce our false color maps.

RESULTS AND DISCUSSION

We used the data acquisition and manipulation methods described here to analyze a number of different tissues and a number of different areas of each tissue. Samples were derived from healthy and diseased prostate, liver, lung, and cervix biopsies. We demonstrated the sensitivity and specificity of the spectroscopic and computational methods to distinguish tissue types and states of disease.
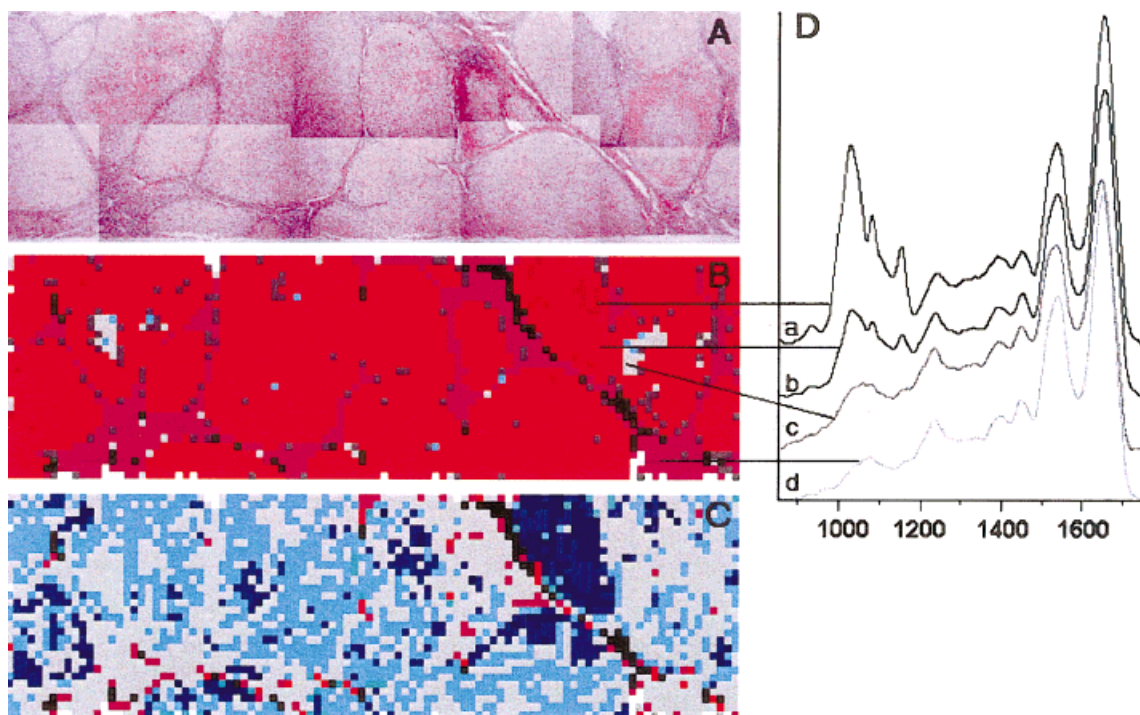
The spectra of the different tissue types (con-

Figure 3. (A) A photomicrograph of a 7.5×2.3 mm^2 section of H&E stained cirrhotic liver tissue. (B) A false color IR-MSP map of cirrhotic liver tissue imaged at 75×75 μm^2 spatial resolution with the vector correlation method. (C) A false color IR-MSP map of cirrhotic liver tissue imaged at 75×75 μm^2 spatial resolution with the Euclidean distance method. (D) Characteristic spectra from (B).

nective tissue, smooth muscle, glands, ducts, blood vessels, etc.) encountered in tissue mapping experiments differ in the total intensity, the amide I/amide II intensity ratio (indicative of variations in structural vs. metabolic proteins), the protein/nucleic acid ratio (indicative of cell proliferation), and other factors. In addition, large spectral variations due to the presence or absence of glycogen may be observed in certain tissues. However, the differences are generally quite small, particularly if the spectra are collected from relatively large areas such as 75×75 μm^2. Because cells in the tissues reported below may cover an area as small as 75–300 μm^2, the selected aperture nearly always samples more than one cell and frequently more than one cell type. This averaging causes homogenization of observed spectra.

Nevertheless, even at a pixel area of 75×75 μm^2, an enormous amount of tissue architectural detail can be discerned from the IR false color maps. Figure 3 shows data of a large section (7.5×2.3 mm^2) of cirrhotic liver tissue mapped at a spatial resolution of 75×75 μm^2. Thus, 3000 (100

$\times$ 30) pixels were collected at a total data acquisition time of about 5 h.

Liver cirrhosis is a condition that arises from chronic metabolic, toxic, microbial, viral, circulatory, and neoplastic hepatic injury. The result is a destruction of the normal hepatic architecture that is replaced by regenerating hepatocyte nodules that are encompassed by fibrous septa. The fibrosis develops in response to inflammation (inflammatory cells) or direct toxic insult. Because the hepatic architecture is distorted, there is necessarily a reorganization of vascular and biliary connections. As a result, a common feature of cirrhosis is the presence of inflammatory cells and proliferating bile ductules.

Figure 3(A) is a composite of 10 individual photomicrographs of a section of cirrhotic liver tissue measuring about 7.5×2.3 mm^2. This panel distinctly shows the fibroconnective tissue bands that encapsulate the liver nodules. Figure 3(B) shows the same tissue area analyzed by IR spectral mapping using the method defined by eq. (3), which is the most sensitive to relatively subtle spectra changes. The correspondence of the tissue
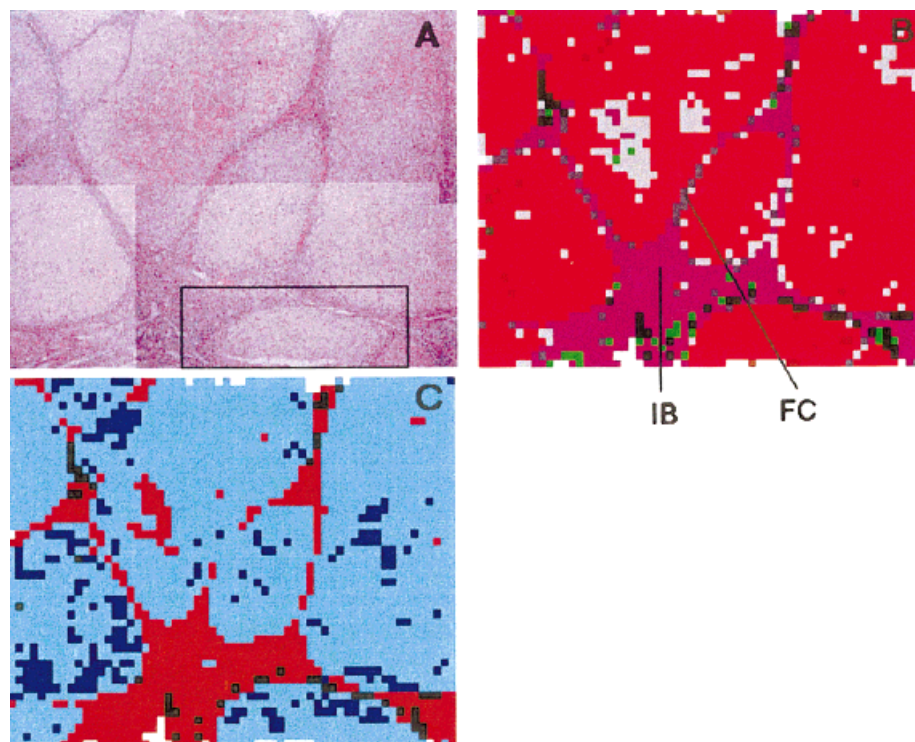
Figure 4.   (A) A photomicrograph of a 2.5×2.3 mm^2 section of H&E stained cirrhotic liver tissue. The rectangular area is the section imaged in Figure 5.   (B) A false color IR-MSP map of cirrhotic liver tissue imaged at 50×50 μm^2 spatial resolution with the vector correlation method. (C) A false color IR-MSP map of cirrhotic liver tissue imaged at 50×50 μm^2 spatial resolution with the Euclidean distance method. FC, fibroconnective tissue; IB, inflammatory and bile duct proliferative tissue.

architectural features observed visually [Fig. 3(A)] and in the IR spectral map [Fig. 3(B)] is immediately obvious.

Because the image analysis method utilized here yields characteristic spectra of physical significance, it is interesting to compare these spectra for the anatomical regions shown. The vast majority of the 3000 pixels can be characterized by one of four spectra [Fig. 3(D)]. These spectra are characteristic for high glycogen hepatocytes, low/medium glycogen, connective tissue, and cellular components. The assignment of these spectra was accomplished by studies of model compounds and spectra of individual, well-defined cells.

This analysis indicates that the regions around the fibrous septa show relatively homogeneous spectral patterns, which are shown in purple in Figure 3(B); however, the spectra observed in the fibrous tissue areas are not those usually associated with connective tissue [collagen, cf. trace c, Fig. 3(D)] but rather with cellular material [trace d, Fig. 3(D)] such as bile ductules and inflamma-

tory cells. At this spatial resolution (75×75 μm^2) the cellular components, rather than the fibroconnective tissue, dominate the averaged spectral pattern observed. However, at better spatial resolution more detailed spectral information is available (see below).

Figure 3(C) shows the same data set analyzed via the Euclidean method [eq. (1)] in the original spectral, rather than second derivative, space. This analysis method is more sensitive to the relative intensity variation of the spectra; therefore, it is particularly sensitive to glycogen variations. A number of nodules have extremely high glycogen content (dark blue), medium glycogen content (light blue), and low or no glycogen (gray). The glycogen content was not detectable in the H&E stained section, but it was demonstrated via a periodic acid/Schiff base stain specific for glycogen.[3] This method of analysis is less sensitive to band shapes than to overall intensity variations between the amide I and low frequency regions; thus, it does not distinguish low glycogen hepato-
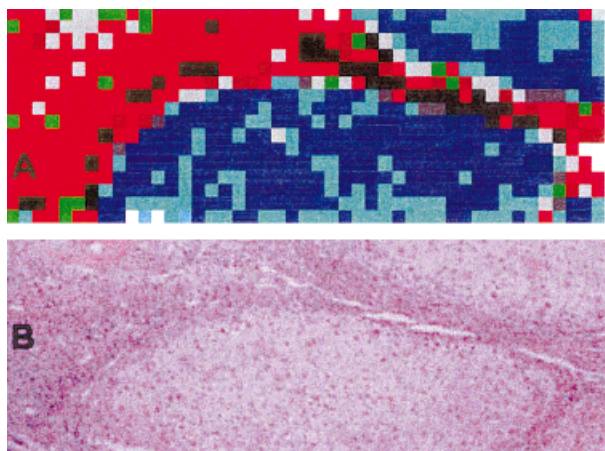
Figure 5. (A) A photomicrograph of a 0.5×0.3 mm^2 section of H&E stained cirrhotic liver tissue. (B) A false color IR-MSP map of cirrhotic liver tissue imaged at 33×33 μm^2 spatial resolution with the vector correlation method.

cytes from the spectral pattern found in the fibrous materials.

Figure 4 shows the left quarter of Figure 3 imaged at 50×50 μm^2 pixel size. Figure 4(A) is again the H&E stained visual image, which is about 2.5×2.3 mm^2 in size. Figure 4(B) shows the IR spectral map obtained using the vector correlation method. At this spatial resolution one can observe the connective tissue spectrum in the fibroconnective areas (FC, gray) and the inflammatory cell and bile duct components in the large area between liver nodules (ICB, purple). We analyzed this data set using the Euclidean distance method and found, as in Figure 3, that low glycogen and connective tissue cannot be distinguished reliably; however, this method yields a distribution of the glycogen-rich hepatocytes in a given lobule.

Figure 5 shows a lower left liver nodule (rectangle in Fig. 4) imaged at 33×33 μm^2 spatial resolution. At this resolution, a number of novel features are observed. For example, in the fibroconnective septa, there is more heterogeneity of the spectra patterns, which is in agreement with various staining results that demonstrate the presence of inflammatory cells and bile duct proliferation. Furthermore, in the liver nodule shown in the lower half of Figure 5, the spectral features of the collageneous matrix in which the hepatocytes are embedded become visible. This aspect is discussed below.

Because the increased spatial resolution reduces the averaging in the observed characteris-

tic spectra, a larger number of these was obtained. The characteristic spectra corresponding to Figure 5 are shown in Figure 6. The top four traces shown in Figure 6 depict the spectra of liver sections of various glycogen content. The spectral region between 900 and 1150 cm^{-1} is dominated by the C—O stretching and C—O—H deformation vibrations of glycogen. Spectral trace D exhibits a distinctive collagen shoulder at 1202 cm^{-1} (also observed in trace G). Thus, we concluded that this spectrum is that of hepatocytes averaged with the connective tissue matrix into which the hepatocytes are embedded. This trace is observed for the light blue areas in the lower liver lobule in Figure 5.

Traces E and F in Figure 6 present the spectra observed in the fibroconnective tissue areas. However, these spectra were previously associated with cellular material such as inflammatory cells; thus, we believe that these spectral traces are due to the bile duct proliferation and inflammatory response that were demonstrated via special histochemical staining procedures.[3,4] Traces G–K in
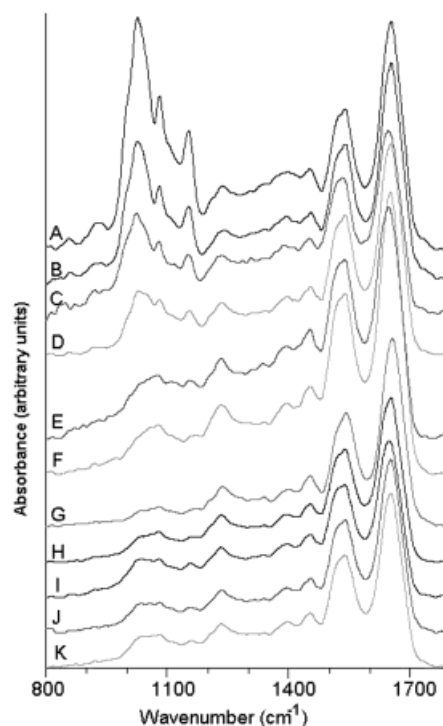

Figure 6. Characteristic spectra of Figure 5. for glycogen-containing hepatocytes (traces A–C), a hepatocyte/collagen mixture (trace D), cellular materials (inflammatory and bile duct cells, traces E, F), collagen (traces G, H), and collagen with minute amounts of glycogen-containing hepatocytes (traces I, K).

Figure 6 show the spectra of the edges of the fibroconnective septa with various amount of hepatocyte spectra added. Thus, these spectra are those of collagen (traces G and H) with small amounts of glycogen added (traces I–K).

CONCLUSIONS

We demonstrated that IR spectral maps contain an enormous amount of information on the nature of the cells that make up a given pixel in tissue. The method of analysis introduced here is particularly suited for correlating the observed spectra with the pathological features of the tissue, because real, characteristic spectra are derived, not abstract combinations of spectral features (such as principal components).

REFERENCES

1. Chiriboga, L.; Xie, P.; Yee, H.; Vigorita, V.; Zarou, D.; Zakim, D.; Diem, M. Biospectroscopy 1998, 4, 47–53.
2. Chiriboga, L.; Xie, P.; Yee, H.; Zarou, D.; Zakim, D.; Diem, M. Cell Mol Biol 1998, 44, 219–229.
3. Chiriboga, L.; Yee, H.; Diem, M. Appl Spectrosc 2000, 54, 1–8.
4. Chiriboga, L.; Yee, H.; Diem, M. Appl Spectrosc 2000, 54(4).
5. Lasch, P.; Naumann, D. Cell Mol Biol 1998, 44, 189–202.
6. Mansfield, J. R.; McIntosh, L. M.; Crowson, A. N.; Mantsch, H. H.; Jackson, M. Appl Spectrosc 1999, 53, 1323–1330.
7. Lewis, E. N.; Kidder, L. H.; Arens, J. F.; Peck, M. C.; Levin, I. W. Appl Spectrosc 1997, 51, 563–567.
8. Mendelson, R.; Paschalis, E. P.; Boskey, A. L. J Biomed Opt 1999, 4, 14–21.
9. Freeman, J. Infrared Imaging Applications in Minimally Invasive Surgery, Advanced Technology Applications to Combat Casualty Care; U.S. Army Medical Research and Material Command, 1998.
10. Bruker Analytische Messtechnik, GmbH. OPUS/IR Reference Manual, Version 2.0; Bruker Analytische Messtechnik, GmbH: Karlsruhe, Germany, 1995.
11. Pevzner, A.; Diem, M. unpublished data.
12. Savitzky, A.; Golay, M. J. E. Anal Chem 1964, 36, 1627–1639.
13. Lewis, E. N. Application Note 110; Spectral Dimensions, Inc.: Olney, MD, 1999.
14. Liang, X.; Andrews, J. E.; deHaseth, J. A. Anal Chem 1996, 68, 378–385.
15. Galactic Industries, Corp. PLSplus/IQ for Grams/32 and Grams/386: Add-on Application; Galactic Industries, Corp.: Salem, NH, 1996.
16. Helm, D.; Labischinski, H.; Schallen, G.; Naumann, D. J Gen Microbiol 1991, 137, 69–79.